Compact Integrated Full-Duplex Gap Waveguide-Based Radio Front End For Multi-Gbit/s Point-to-Point Backhaul Links at E-Band

Compact Integrated Full Duplex Gap Waveguide Based Radio Front-end For Multi-Gbit/s Point-to-Point Backhaul Links at E-band

Abbas Vosoogh, Milad Sharifi Sorkherizi, Vessen Vassilev, Ashraf Uz Zaman, Zhongxia Simon He, Jian Yang, Ahmed A. Kishk, *Fellow, IEEE,* and Herbert Zirath, *Fellow, IEEE*

***Abstract*—This paper presents the design and realization of a high data rate radio front-end module for point-to-point backhaul links at E-band. The design module consists of four vertically stacked unconnected metal layers without any galvanic and electrical contact requirements among the building blocks, by using gap waveguide technology. The module components are a high gain array antenna, diplexer, and circuitry consisting of a transmitter (Tx) and a receiver (Rx) monolithic microwave integrated circuits (MMICs) on a carrier board, which are successfully integrated in one package with a novel architecture and a compact form. The diplexer consists of two direct-coupled cavity bandpass filters with channels at 71-76 GHz and 81-86 GHz with a measured return loss of 15 dB and an isolation greater than 50 dB. A wideband 16×16 slot array antenna with a measured gain of more than 31 dBi is used to provide high directivity. The measured results show that the packaged transmitter provides a conversion gain of 22 dB and 20 dB at 76 GHz and 86 GHz, respectively, with an output power of 14 dBm and 16 dBm at 1-dB gain compression point, at the same frequencies. The packaged receiver shows an average conversion gain of 20 dB at 71-76 GHz and 24 dB at 81-86 GHz bands. A real-time wireless data transmission is successfully demonstrated with a data rate of 8 Gbit/s using 32 quadrature amplitude modulated signal over 1.8 GHz channel bandwidth with spectral efficiency of 4.44 bit/s/Hz. The proposed radio front-end provides the advantages of low loss, high efficiency, compact integration, and a simple mechanical assembly, which makes it a suitable solution for small cell backhaul links.**

***Index Terms*—frequency division duplex (FDD), gap waveguide, integration, millimeter-wave, slot array antenna, wireless communication.**

I. Introduction

THE increasing demand for higher data traffic and speed in mobile cellular networks leads to a need for higher bandwidth and data rate in the backhaul side of the network. Nowadays, smartphones are not only used for voice calls, but also employed for applications that involve an extensive data consumption. For example, for a typical fourth-generation (4G) cellular network the required backhaul data exceeds 250 Mb/s [1]. There is a demand for ultra-high data rate backhaul point-to-point wireless links as a flexible and cost-effective alternative to fiber optic networks to provide multi Gbit/s speed for the fifth-generation (5G) wireless cellular networks. The millimeter-wave frequency band (30-300 GHz), has recently got a lot of attention to provide high capacity backhaul wireless links with high speed and low latency.

Millimeter-wave wireless communication systems suffer from high path loss, atmospheric absorption and they are vulnerable to weather conditions and precipitation [1]. All these factors limit the hop length to a couple of kilometers at millimeter-wave frequencies. However, an atmospheric window exists at E-band (71-76 GHz and 81-86 GHz) with low atmospheric attenuation of around 0.4 dB/km [1]. This makes the E-band a potential candidate to provide multi-Gbit/s data transfer and complements the conventional wireless links that operate in the microwave frequency band. In [2] path loss measurements during ten months versus weather conditions for a 1 km link at 71-76 GHz is presented. The measured attenuation for the rain rate of 20 mm/h and 40 mm/h in one kilometer is estimated to be 10 dB and 16.4 dB at 86 GHz, respectively, which are with good agreement with the ITU-R attenuation model in [3].

A lot of effort has been devoted for developing complete transmitter (Tx) and receiver (Rx) chipsets with different technologies at E-band during the past few years. In [4] an E-band Tx in SiGe BiCMOS technology is presented with an average conversion gain of 23 dB over 71-86 GHz frequency band and maximum 1-dB compression output power of 15 dBm at 72 GHz. A wireless data transmission of 10.12 Gbit/s with 64-QAM modulation over 2 GHz channel is demonstrated using bench-test measurement setup. In [5] 6 Gbit/s data transmission by aggregating 4 channels with 625 MHz bandwidth has been demonstrated by using 8PSK modulation with bench-test measurement setup. A 2.4 bit/s/Hz spectral efficiency has been achieved in the 81-86 GHz frequency band. A 10 Gbit/s data transmission of 16-QAM modulated signal at 70/80 GHz band is shown in [6] with spectral efficiency of 2 bit/s/Hz. Packaged eWLB SiGe transceiver chipsets are presented in [7] for wireless backhaul application in V- and E-band. A maximum data transmission of 20 Gbit/s with spectral efficiency smaller than 5 bit/s/Hz using 32-QAM modulation is reported in that work.

This paper presents for the first time an E-band full duplex radio front-end module for multi-Gbit/s point-to-point wireless

Manuscript received September 11, 2018; revised December 15, 2018; accepted Month DD, YYYY

A. Vosoogh, A. Uz Zaman, and J. Yang are with the Electrical Engineering Department at Chalmers University of Technology, Gothenburg, Sweden (e-mails: abbas.vosoogh@chalmers.se).

M. Sharifi Sorkherizi and A. A. Kishk are with the Electrical and Computer Engineering Department, Concordia University, Montreal, Canada.

V. Vassilev, Z. S. He, and H. Zirath are with the Department of Microtechnology and Nanoscience at Chalmers University of Technology, Gothenburg, Sweden.

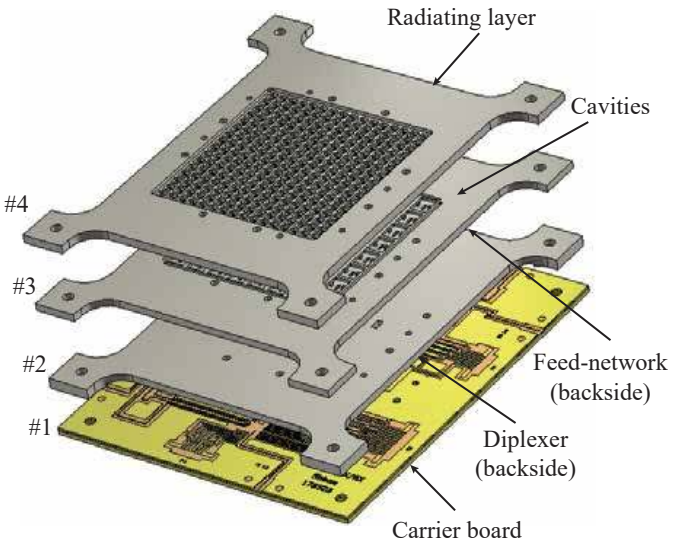

Fig. 1. Configuration of the proposed compact radio front-end.

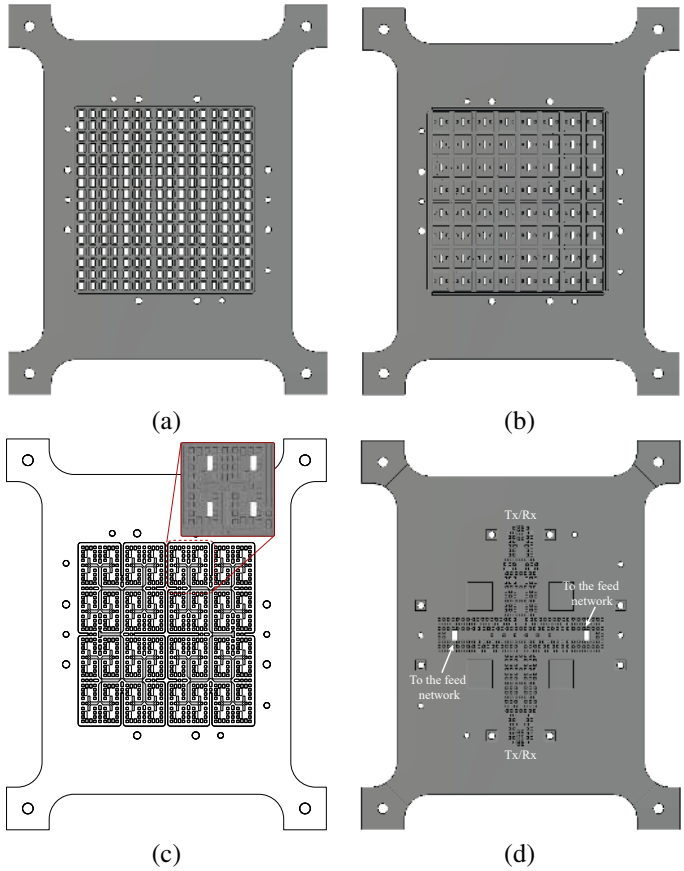

Fig. 2. Detail illustration of each layer. (a) Radiating slots. (b) Cavities to feed the slots on topside of layer 3. (c) View of the bottom side of layer 3 containing the corporate feed-network. (d) Diplexer on the bottom side of layer 2.

link applications based on gap waveguide technology. We present a compact integration of passive and active components, as well as a system packaging solution based on gap waveguide technology with a flexible mechanical assembly. An E-band radio transceiver module consisting of a high gain array antenna, a diplexer, and Tx/Rx chipsets (all in one package) is designed with the capability of sending and receiving data simultaneously at the 71-76 GHz and the 81-86 GHz bands with a frequency division duplex (FDD) transmission scheme. The design procedure and performance verification of each building block, i.e., diplexer, 16×16 slot array antenna, circuitry, and packaging, are presented. In this paper, we have shown the impressive packaging, and integration features that gap waveguide technology offers to build up a complex system with simple mechanical assembly.

Section II presents the overall configuration and characteristics of the proposed E-band integrated radio front-end module by using the gap waveguide technology. The design and performance evaluation of a special hybrid diplexer-splitter is presented in Section III. In Section IV the design and experimental evaluation of a 16×16 array antenna and its integration with the diplexer are described. Section V deals with the carrier board design and the Tx and Rx MMICs packaging and performance evaluation. The implementation of a point-to-point real-time wireless link with the proposed compact integrated radio modules is demonstrated in Section VI. Finally, some concluding remarks are given in Section VII.

II. Integrated Radio Front-end Module

The configuration of the proposed E-band integrated radio front-end is shown in Fig. 1. The module consists of a tightly integrated high gain array antenna, a 5^{th} order diplexer, and Tx and Rx chipsets on a carrier board in four distinct layers, where each layer has different functionality. The layers are vertically stacked up and integrated in a compact form. The proposed module has total dimensions of 110 mm×90 mm ×8.5 mm.

The bottom layer acts as a carrier printed circuit board (PCB) for two complete highly integrated GaAs transmitter and receiver MMICs. We have used commercially available Tx MMIC from Gotmic AB (part No. gTSC0023) with on-wafer 25 dB gain and 16 dBm 1-dB gain compression output power. The Tx has a direct conversion architecture with a ×6 frequency multiplier. It covers 71-86 GHz frequency band with IF frequency bandwidth of DC-12 GHz in the input LO frequency band of 11.8-14.3 GHz. Two receiver MMICs are used to cover the frequency band of 71-76 GHz (part No. gRSC0012) and 81-86 GHz (part NO. gRSC0013) from the same manufacturer. The Rx MMICs are highly integrated chipsets with a ×6 frequency multiplier, an in-phase and quadrature (IQ) mixer, IF and low noise amplifiers with approximately 25 dB conversion gain and 6 dB noise figure. The Tx and Rx MMICs are placed on the carrier board that consists of 100 μm Liquid Crystal Polymer (LCP) substrate on a 1 mm copper plate. More details of the design and layout of the carrier board are presented in Section V.

A 5^{th} order hybrid diplexer-splitter is designed on the bottom side of layer 2 in groove gap waveguide (GGW). The Tx and Rx MMICs are wire-bonded to microstrip lines, and the RF signals are coupled to the diplexer via a microstrip to GGW transition. We have tried to minimize the length where the RF signal propagates within the microstrip lines to

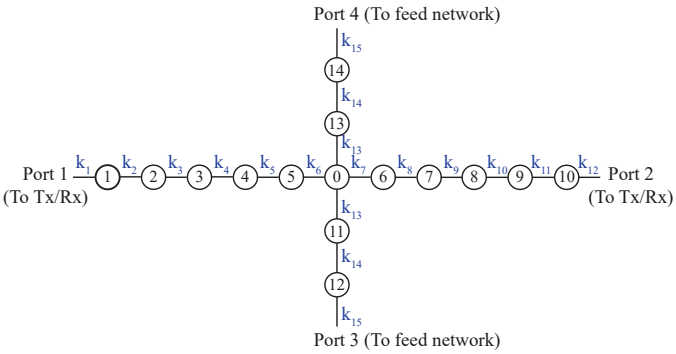

Fig. 3. Coupling diagram of a hybrid diplexer-splitter with a 5^{th} order divider network and 5^{th} order channel filters.

TABLE I
OPTIMIZED PARAMETERS OF THE COUPLING MATRIX OF THE HYBRID DIPLEXER-SPLITTER WITH A DIVIDER NETWORK (REFERS TO FIG. 3)

Parameter	value	Parameter	value (GHz)
k_1	0.0932	f_0	80.057
k_2	0.0626	f_1	73.051
k_3	0.0434	f_2	73.252
k_4	0.0415	f_3	73.367
k_5	0.0482	f_4	73.583
k_6	0.0959	f_5	74.806
k_7	0.0801	f_6	83.295
k_8	0.0461	f_7	83.366
k_9	0.0398	f_8	83.289
k_{10}	0.040	f_9	83.277
k_{11}	0.0577	f_{10}	83.264
k_{12}	0.0886	f_{11}	79.57
k_{13}	0.106	f_{12}	80.241
k_{14}	0.2011	f_{13}	79.587
k_{15}	0.2031	f_{14}	80.241

reduce the high dielectric and conductive losses of microstrip transmission lines. The designed diplexer has two channels (at 71-76 GHz and 81-86 GHz) with 5 GHz bandwidth. In order to achieve a compact design, the output of the diplexer is directly connected to a power divider, so that the diplexer acts as the first stage of the power division for corporate feeding of the array of slots on the top layer. Fig. 2(d) shows the hybrid diplexer-splitter on the backside of layer 2.

A distribution feed network is designed on the backside of layer 3. The outputs of the diplexer are coupled to the next layer, i.e., the feed network, via a right-angle GGW to rectangular waveguide transition. The feed network is designed in ridge gap waveguide (RGW) in order to accommodate the corporate feeding of the array antenna elements within a limited available space. We have used a 2×2 cavity-backed slot subarray as radiating element of the designed array antenna. The radiating part consists of 8×8 subarrays (16×16 slots in total), where they are fed by the same phase and amplitude. The subarrays are formed in two distinct layers, i.e., the cavities (placed at the top side of layer 3) and the radiating layer (on layer 4). The topside of layer 3 contains 8×8 cavities that feed the 16×16 slots of layer 4 uniformly. The geometry of the feed network and the radiating elements are shown in more detail in Fig. 2(a), (b), and (c).

In the proposed module shown in Fig. 1, the different layers do not need to have any electrical and galvanic contact, and a small gap between each layer would not affect the electrical performance of the module. All field leakages and unwanted modes have been suppressed by using a stopband produced by an electromagnetic bandgap (EBG) structure realized in gap waveguide technology, that was introduced for the first time in [8], [9]. Therefore, despite of the H-plane split-block configuration of the proposed waveguide module, electrical and galvanic contacts among the layers are not required, which is the major advantage compared to the conventional hollow waveguide technology.

In gap waveguide technology a guiding structure, such as groove [10], ridge [9], or inverted microstrip line [11], is created between two parallel plates by using an EBG structure, i.e., a periodic pin texture, to control the direction of propagation and preventing any field leakage without the need of electrical contact between the building blocks. This provides a flexible and cost-effective fabrication, and mechanical assembly. The advantages of this technology to design high gain millimeter-wave array antennas [12]–[16], bandpass filters [17]–[24], array antenna and passive components integration [25]–[27] have been shown in the past few years.

In the present work, we try to show the advantages of gap waveguide technology from the complete system design, integration, and packaging point of views. Due to the complexity of the proposed integrated radio front-end module, we have initially designed and verified the performance of each building block separately. The following sections present the detailed design and measured performance for each critical components within the system.

III. HYBRID DIPLEXER-SPLITTER DESIGN

In this section, the design and optimization of the hybrid diplexer-splitter that is used in the module are explained. We try to keep this section brief and refer the reader to the references for more detailed technical discussion. The proposed design is based on the prototype developed in [28] and [25]. However, due to the required wideband performance of the diplexer for the current work, we had to expand the design to a more complicated geometry, and as a result, some minor modifications were required to the original methodology. The diplexer channels are required to be allocated at 71-76 GHz and 81-86 GHz with 20 dB return loss and provide at least 50 dB isolation. This translates to 19.2% of overall fractional bandwidth for the diplexer. Such a wide bandwidth requires strong couplings especially in the divider section of the device. After calculating the required polynomial degrees of the filters to achieve the isolation, we tried to use a similar geometry as the one shown in [28], with a single resonator node as a divider to implement the required electrical specifications. By doing this, we understood that this geometry is unable to provide the required bandwidth for the common couplings. To overcome this issue, we expanded the divider network to be constituted of five resonators as shown in Fig. 3 to decrease the couplings for each element. Port 1 and 2 are the outputs of the channel filters while port 3 and 4 are the inputs of the divider section.

The next step is to calculate the lumped element network of the hybrid diplexer-splitter. In [28] we proposed a goal

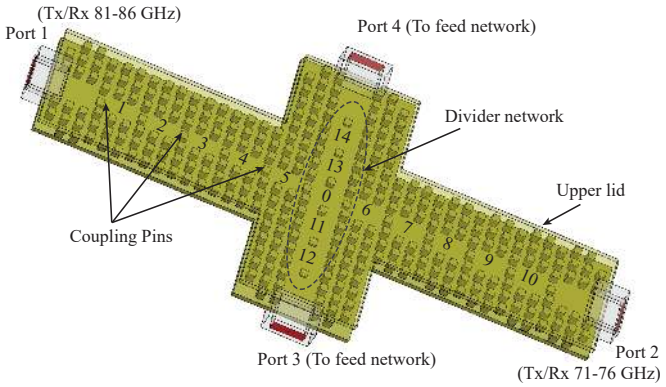

Fig. 4. Geometry of the proposed hybrid diplexer-splitter.

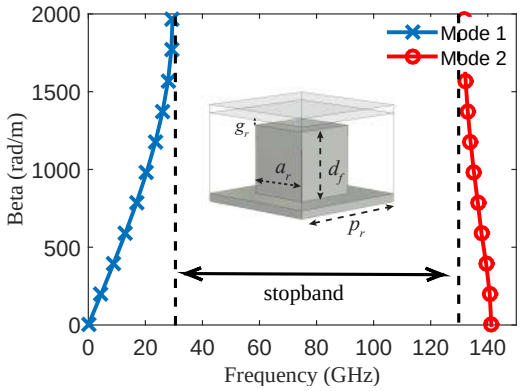

Fig. 5. Dispersion diagram of the infinite periodic pin unit cell (d_f = 0.7 mm, a_r = 0.64 mm, g_r = 0.04 mm, and p_r = 1.32 mm).

function that extract the Coupling Matrix (CM) of the diplexer-splitter by applying an optimization routine, while eliminating the spurious pole between ports 3 and 4. Since we need a divider with an equal 3 dB power division, the divider section is symmetric with respect to the center. It is possible to design the hybrid diplexer-splitter with any desired power division value by removing this symmetry and modifying the goal function to represent the division characteristic. The instruction to choose the correct initial values in order to achieve a fast convergence of the routine is already available in [28] and [25]. The calculated CM is shown in TABLE I. To avoid the ambiguity regarding the coupling bandwidth, the de-normalized k coupling is presented along with the resonant frequencies.

To convert the parameters in TABLE I to the normal CM parameters, one can use the next equation.

$$M_{ij} = K_{ij}/FBW \tag{1}$$

in which FBW is the fractional bandwidth. It is important to remark that the diplexer has three different FBW. For the common section (k_{13}-k_{15}) the FBW is computed by including the overall bandwidth of the diplexer (f_1=71 GHz, f_2=86 GHz). We call this as FBW1=0.192. For k_1-k_6, FBW is computed by considering f_1=71 GHz and f_2=76 GHz. This will give us FBW2=0.068. Finally, for k_7-k_{12} the operating bandwidth is from f_1=81 GHz to f_2=86 GHz. Therefore, this

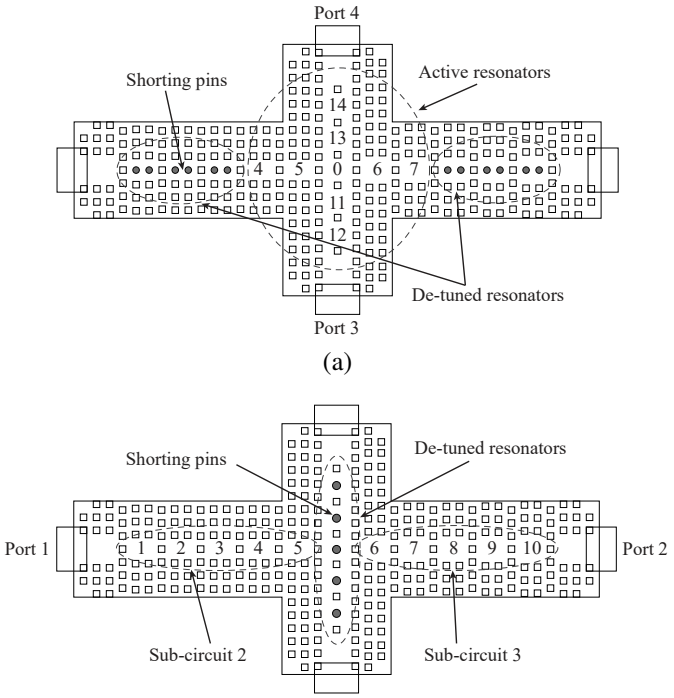

Fig. 6. Sub-circuits that are used to implement the CM to the physical model. (a) Sub-circuit 1 for calculating the divider network cavities dimensions. (b) Sub-circuits 2 and 3 for calculating the channel filter cavities dimensions.

provides FBW3=0.06. We can translate the input couplings to input resistances using the equation:

$$R = M^2 \tag{2}$$

$$Q_e = \frac{1}{R \cdot FBW} \tag{3}$$

The external Q-factor can be calculated by using the classic formula expressed in (3). Equations (1-3) are taken from [29] where further clarifications about these formulas can be found. Furthermore, equation (4) has been used to convert the diagonal entries of the CM to physical resonant frequencies:

$$f_k = \frac{f_0}{2}\left[M_{kk} \cdot FBW + \sqrt{\left(M_{kk} \cdot FBW\right)^2 + 4}\right] \tag{4}$$

which f_0 is the center frequency calculated by:

$$f_0 = \sqrt{f_1 f_2} \tag{5}$$

Similarly, each resonator has a different FBW and f_0 depending on its position in the circuit. Resonators 0-13-14 are in the FBW1 Region, while resonators 1-5 are within the FBW2. The rest of the resonators are allocated in the FBW3 region. Three different f_0 values should be calculated similarly. This explains why using a de-normalized coupling, and the resonant frequency is easier for this design.

The calculated CM is meant to be implemented by using the geometry shown in Fig. 4. The structure is based on groove gap waveguide that consists of a semi-periodic array of metallic pins along with a metallic top plate. The top plate is

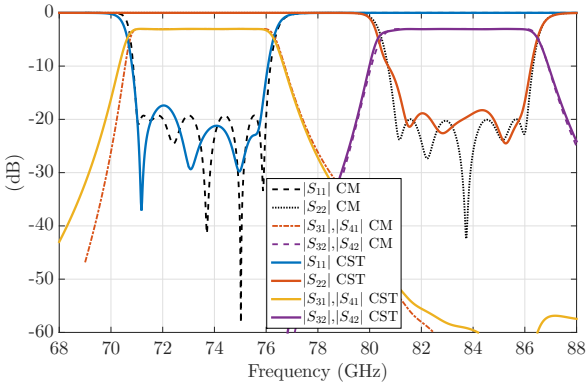

Fig. 7. Response of the coupling diagram in Fig. 3 with the parameters of TABLE I, along with the EM model response.

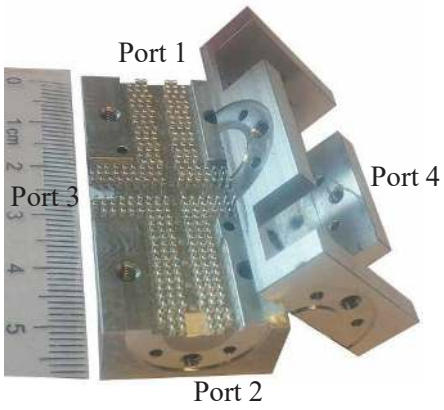

Fig. 8. Fabricated diplexer.

transparent in Fig. 4 for a better visualization of the inner part of the design. Metallic pin dimensions are designed to create a bandgap that can confine the field in the cavities without the need of galvanic contact among the top and lower plate. Fig. 5 shows the dispersion diagram of a pin unit cell with infinite periodic boundary conditions, by using the Eigenmode solver CST Microwave Studio EM simulation software. The given periodic pin unit cell provides a stopband that covers the whole frequency band of interest. The resonators are created by removing two adjacent pins, and the resonant frequency is controlled by moving the surrounding pins closer or away to the center of the cavity, thereby by changing the width of the cavities. The height of the pins remains constant except for the pins that are responsible for controlling the couplings. The coupling value between each cavity is controlled by the height of a short pin between the resonators.

To translate the lumped model of Fig. 3 to the EM model in Fig. 4, an efficient technique is required since gap waveguide technology has a complex structure and therefore optimizing with full-wave simulations is time-consuming. The method proposed in [30] is based on dividing the structure in many sub-circuits and using the delay response of each sub-circuit to extract the CM of them. By using the Space Mapping proposed in [31], each sub-circuit is optimized in an iterative procedure that can converge in a few iterations. Later, dimensions of the

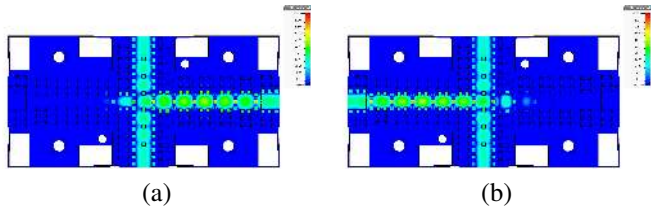

Fig. 9. Simulated E-field within the pin texture of the proposed diplexer at (a) 73.5 GHz, and (b) 83.5 GHz.

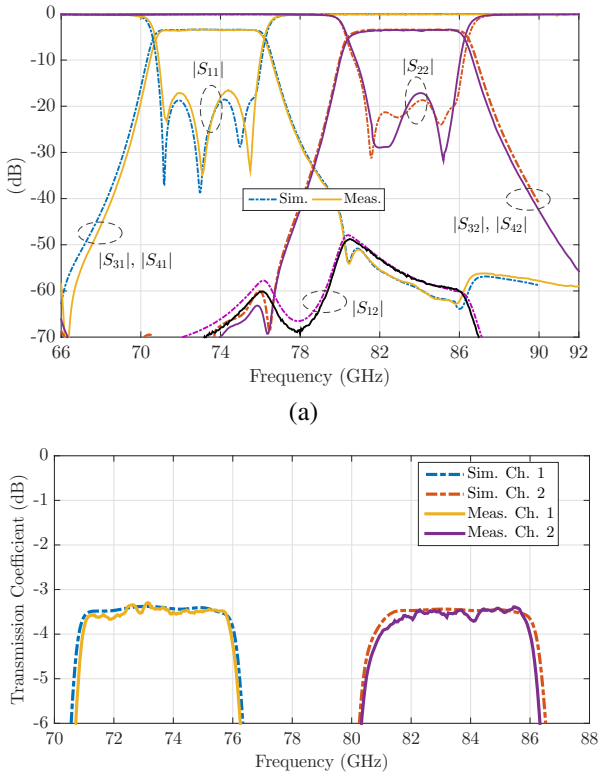

Fig. 10. (a) Measured and simulated performance of the designed diplexer. (b) Zoomed view of the simulated and measured transmission coefficient of the two channels.

cavities and coupling pins from all the sub-circuits are used to generate the complete model. Following this procedure, the geometry yields a very close response compared to the designated CM without performing any full-wave EM optimization.

We have used three sub-circuits to calculate all the dimensions of the proposed hybrid diplexer-splitter in Fig. 4. Sub-circuit 1 consists of resonators 0, 4-7 and 11-14, which include the divider section and two cavities from each channel as shown in Fig. 6 (a). The rest of the resonators are detuned by having shorting pins at their centers. In the sub-circuits 2 and 3 (Fig. 6 (b)), the remaining cavities for each filter are contained in the circuits. It is important to note that sub-circuit 2 and 3 can be solved at the same time, because they are isolated from each other by the detuned cavities between them. Sub-circuits are chosen in a way that they have an overlap with each other. This is done intentionally to consider the loading effect on the last resonator of each. This is further explained in [30]. After calculating all the dimensions by following the procedure in

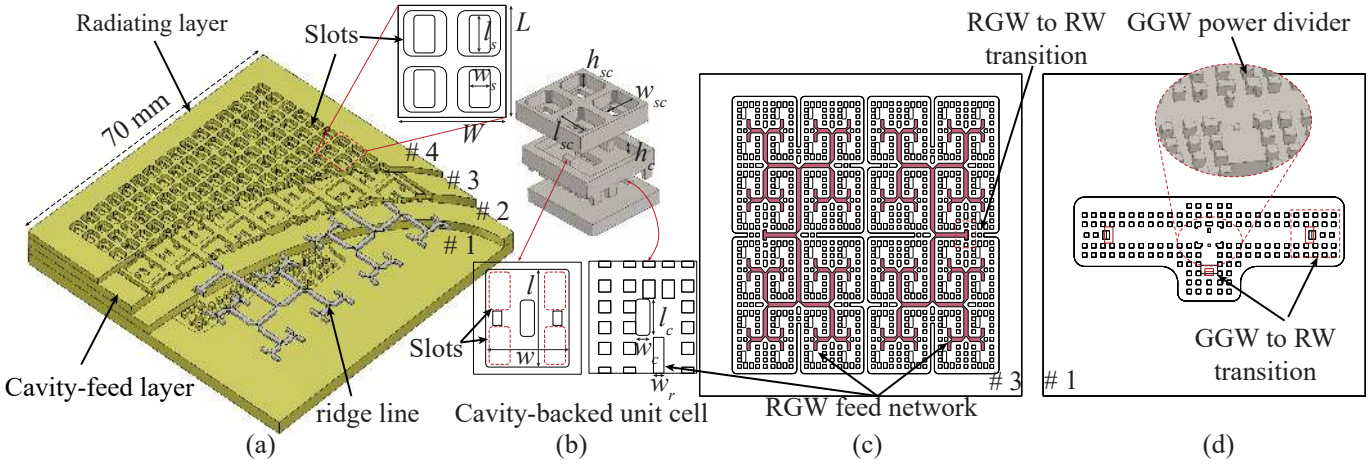

Fig. 11. The designed multi-layer 16×16 slot array antenna. (a) Different layers configuration. (b) 2×2 cavity-backed slot subarray. (c) Distribution ridge gap waveguide feed network. (d) Bottom layer power divider for experimental evaluation of the designed array.

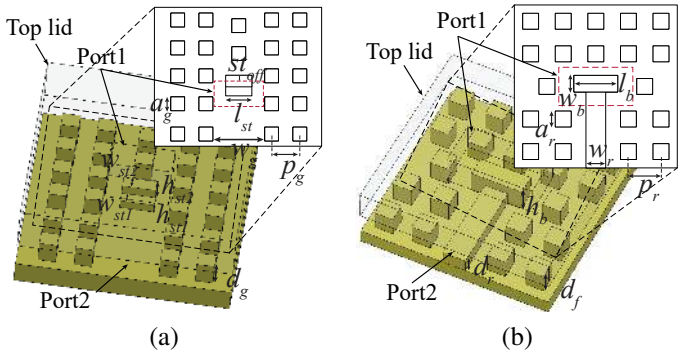

Fig. 12. Configuration of the proposed, (a) Groove gap waveguide (GGW) to rectangular waveguide, and (b) Ridge gap waveguide (RGW) to rectangular waveguide transitions.

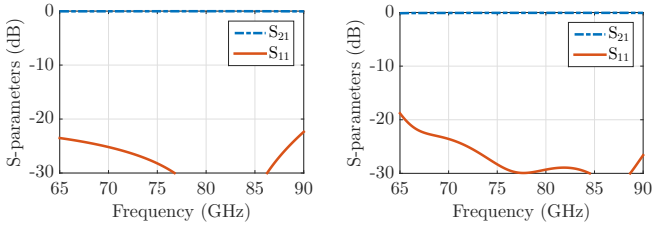

Fig. 13. Simulated performance of the designed transitions. (a) GGW to RW transition. (b) RGW to RW transition.

[25] and [30], the electric response of the diplexer-splitter is simulated which is shown in Fig. 7. We used CST Microwave Studio to solve the EM model. Fig. 7 shows the response of the CM compared to the optimized EM model performance.

In order to verify the design procedure and simulations, a prototype is fabricated by Computer Numerical Control (CNC) milling in aluminum, as shown in Fig. 8. All the inputs of the fabricated diplexer-splitter are connected to standard WR-12 waveguide flanges. Since the height of the pins (1 mm) are smaller than the height of the standard rectangular waveguide (1.55 mm), we have tapered the inputs in order to reach the same height, as shown in Fig. 8. The simulated E-field distribution within the pin texture of the designed diplexer at 73.5 GHz and 83.5 GHz are shown in Fig. 9. It can be seen that the energy is well confined within the resonators and there is no field leakage, in spite of no electrical contact between the pin texture and the top lid.

Fig. 10 shows the measured and simulated performance of the fabricated diplexer. The measured results are in a very good agreement with the simulated ones. The fabricated prototype shows a tolerance below 8 μm. The measured input reflection coefficients of the two channels are below -17 dB. The measured isolation between the two input ports ($|S_{12}|$) is smaller than 50 dB. The measured isolation between the two channels ($|S_{j1}|, |S_{j2}|$) is also better than 50 dB. Fig. 10(b) shows that the designed diplexer has a low loss performance. The measured transmission coefficients of both channels are better than -3.5 dB, which in an ideal lossless situation should be -3 dB, taking into account the power splitter for the feed network. Therefore, the fabricated prototype shows a maximum of 0.5 dB insertion loss. We remark that in the simulated results, aluminum is used for modeling the structure.

IV. Antenna Design

We have designed a planar array antenna to provide a compact structure and high directivity. We have previously presented several gap waveguide based slot array antennas in different frequency bands in [12], [14], [16], [25]. The radiating element of the array and the design procedure are similar to the mentioned references. In this section we give an overview of the designed slot array and diplexer and antenna integration, followed by experimental verifications.

Fig. 11 shows the configuration of the designed array antenna. It consists of 16 × 16 uniformly excited slots which provide a gain higher than 31 dBi in the 71-86 GHz frequency band. The array antenna shown in Fig. 11 (a) is formed by four stacked up layers, where the layers do not need any electrical contact among them. A 2×2 cavity-backed slot element is used as a subarray, to provide enough space to design a corporate feed network, as shown in Fig. 11 (b). The designed array contains 8×8 subarrays in total. The slots placed on layer 4,

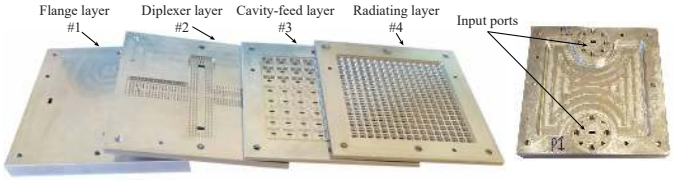

Fig. 14. Fabricated antenna-diplexer prototype.

TABLE II
DIMENSIONS OF THE DESIGNED ARRAY ANTENNA (REFERS TO FIG. 11 AND FIG. 12)

Parameter	Value (mm)
Subarray	
Subarray width in x direction (L)	6.48
Subarray width in y direction (W)	6.23
Width of the slot (w_s)	1.2
Length of the slot (l_s)	2.2
Width of the slot cavity (w_{sc})	2.5
Length of the slot cavity (l_{sc})	2.63
Height of the slot cavity (h_{sc})	0.98
Thickness of the slot layer (t_s)	0.35
Length of the cavity (l)	5.65
Width of the cavity (w)	4.82
Height of the cavity (h_c)	0.75
Width of the coupling slot (w_c)	0.82
Length of the coupling the slot (l_c)	2.1
RGW Feed network	
Width of the ridge (w_r)	0.8
Height of the ridge (d_r)	0.47
Air gap between the pins and the upper lid (g_r)	0.04
Pins period (p_r)	1.32
Width of the pins (a_r)	0.64
Height of the pins in RGW (d_f)	0.7
GGW to RW transition	
Width of the pins in GGW (a_g)	0.83
Height of the pins in GGW (d_g)	1
Air gap in GGW (g_g)	0.1
Pins period in GGW (p_g)	1.7
Length of the step (l_{st})	1.6
Height of the step1 (h_{st1})	0.41
Height of the step2 (h_{st2})	0.86
Width of the step1 (w_{st1})	0.55
Width of the step2 (w_{st1})	0.7
Step offset (st_{off})	0.35
RGW to RW transition	
Length of the metal block (l_b)	1.77
Width of the metal block (w_b)	0.67
Height of the metal block (h_b)	0.81

i.e. the radiating layer, are fed by cavities on layer 3, as shown in Fig. 11 (a). A ridge gap waveguide (RGW) feed network on the backside of layer 3 feeds the cavities via coupling apertures. The configuration of the designed feed network is shown in Fig. 11 (c). The feed network is divided into two parts, where each of them excites half of the radiating slots. The reason for this is that the designed array is going to be integrated with a diplexer which provides the first power division stage in order to achieve a compact integration. For the purpose of testing the array antenna separately, we have designed a groove gap waveguide power divider as shown in Fig. 11 (d). This is made just for performance evaluation and this layer will be later replaced by the designed diplexer-

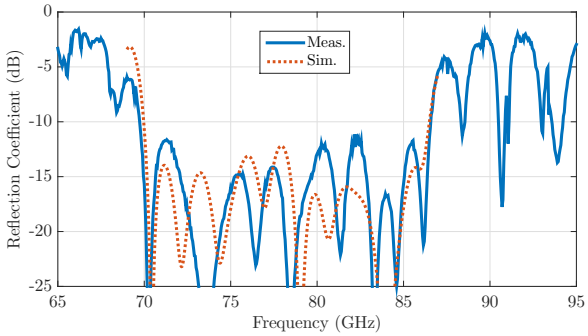

Fig. 15. Comparison of measured and simulated input reflection coefficient of the designed 16×16 slot array.

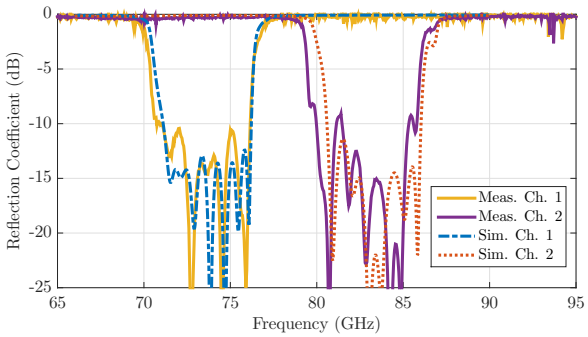

Fig. 16. Measured and simulated performance of the integrated antenna-diplexer.

splitter.

Since the presented antenna has a multi-layer architecture, low loss interconnection and transitions are needed. Fig. 12 shows the two designed transitions used as interconnections of the different layers. The geometry of the proposed vertical transition between a rectangular waveguide (RW) and a groove gap waveguide is shown in Fig. 12 (a). A 90° E-Plane bend is formed by a metal step at the end of the GGW line. This transition is used to couple the energy from the diplexer-splitter to the upper layer where the feed network of the array antenna is located. Fig. 12 (b) illustrates the transition from a rectangular waveguide (RW) to a ridge gap waveguide (RGW) to match the TE_{10} dominant mode of the RW to the quasi-TEM mode of the RGW. The simulated S-parameters of the proposed transitions after optimization are presented in Fig. 13. Both transitions show a wideband impedance matching performance with reflection coefficients below −20 dB over the frequency band of 65-90 GHz. The dimensions of the designed array antenna are presented in Table II. It is worthy to mention that we have used bigger pins with larger periodicity in the diplexer/GGW transition layer to simplify the fabrication.

Fig. 14 shows a fabricated prototype of the integrated antenna-diplexer manufactured by CNC milling in aluminum. The layers are assembled and kept in place by using a few screws. The antenna-diplexer prototype has two WR-12 standard flanges at the backside. The layer 2 (diplexer layer) in Fig. 14 is replaced by the fabricated GGW power divider layer

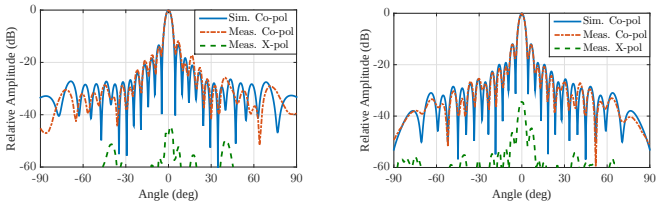

Fig. 17. Simulated and measured radiation patterns of the fabricated antenna-diplexer at center of channel 1 at 73.5 GHz. (a) E-plane, (b) H-plane.

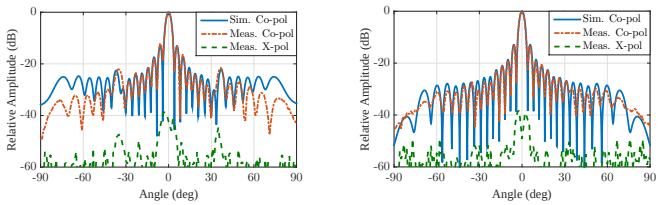

Fig. 18. Simulated and measured radiation patterns of the fabricated antenna-diplexer at center of channel 2 at 83.5 GHz. (a) E-plane, (b) H-plane.

that is shown in Fig. 11 (d), in order to verify the performance of the antenna alone as well.

The simulated and measured input reflection coefficients of the designed 16×16 slot array antenna are presented in Fig. 15, showing a good agreement between simulations and measurements. The measured reflection coefficient is below -11.5 dB in a frequency band of 70-86.5 GHz, which shows a broad impedance bandwidth of 21%. The antenna is measured with a waveguide input port at the bottom as shown in Fig. 11 (d).

Fig. 16 shows the simulated and measured reflection coefficient of the manufactured integrated antenna-diplexer. There is a certain discrepancy in the measured results with respect to the simulations. The measured input reflection coefficient of the upper channel (81-86 GHz) shows a wider passband bandwidth. This could be due to assembly errors, since the fabricated diplexer layer prototype was slightly bent because of mechanical tensions in the fabrication process. Due to the large surface of this layer, the flatness of the layers cannot be guaranteed by a few screws. However, this is not a problem in smaller work-pieces, such as the fabricated diplexer of Section III.

The far-field radiation performance of the fabricated antenna-diplexer is measured in a far-field anechoic chamber. The simulated and measured radiation patterns of the fabricated antenna-diplexer are presented in Fig. 17 and Fig. 18 at the center frequencies of the two channels. As can be seen, the simulated and experimental results are in a good agreement. The fabricated prototype shows good co-polar radiation patterns in E- and H-planes, with a measured cross-polarization better than -35 dB. Fig. 17 and 18 demonstrate that although the designed antenna has a multi-layer architecture with several interconnections and transitions, the radiating slots are excited correctly.

Fig. 19 shows the simulated and measured gains of the

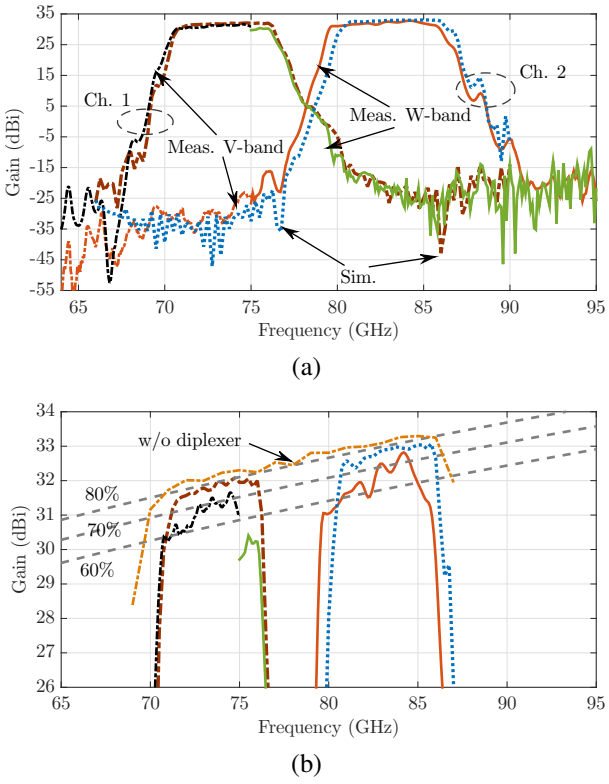

Fig. 19. (a) Simulated and measured gains of the fabricated antenna-diplexer. (b) Zoomed view of simulated and measured gains. The dashed lines are the directivities with 80%, 70%, and 60% aperture efficiencies.

two inputs (as illustrated in Fig. 14) of the manufactured antenna-diplexer. The measurement is done with two V-band and W-band measurement setup to cover the frequency band of interest. The measured results show 55 dB and 50 dB isolation in gain in the 71-76 GHz and 81-86 GHz frequency bands, respectively. A more detailed measured and simulated gain performance of the fabricated antenna-diplexer and the simulated gain of the array antenna without the diplexer is illustrated in Fig. 19 (b). The maximum directivity from an aperture with the same aperture size of the designed antenna with different efficiencies is also presented in Fig. 19 (b). The simulated antenna without the diplexer shows 80% antenna efficiency. The measured integrated antenna-diplexer shows average 31 dB and 32 dB gains in channel 1 and channel 2 at 71-76 GHz and 81-86 GHz, respectively, with an antenna efficiency of around 65%. It is expected that 0.5 dB (as shown in Fig. 10 (b)) drop in the gain and having lower antenna efficiency is due to the extra loss of the diplexer.

V. PCB Carrier Board Design

Fig. 20 shows the designed PCB board to mount the Tx and Rx MMICs and supply the required DC bias voltages. The Tx and Rx dies are attached and wire bonded to the board, as shown in Fig. 20. To minimize the effect of the wire-bond and reduce the losses, we used a matching section at the RF input/output of Rx/Tx MMICs to compensate the inductance of the wire-bond. We have used Liquid Crystal Polymer (LCP) substrate that provides a stable dielectric constant and low loss

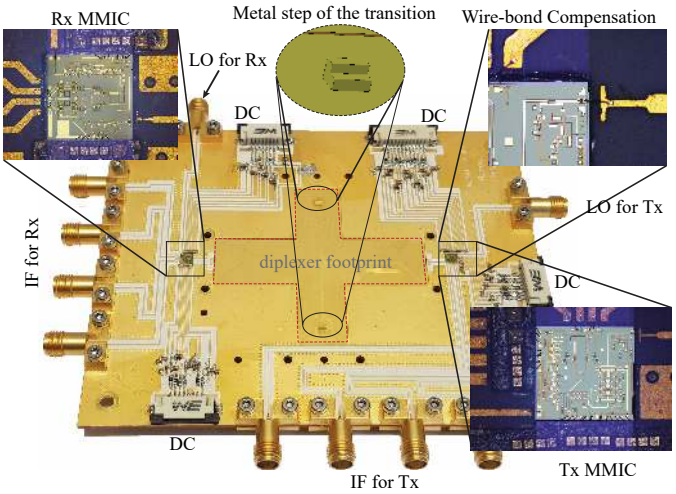

Fig. 20. Carrier board consisting of Tx and Rx MMICs, wire-bond compensation, IF and LO coaxial ports, and microstrip to GGW transitions.

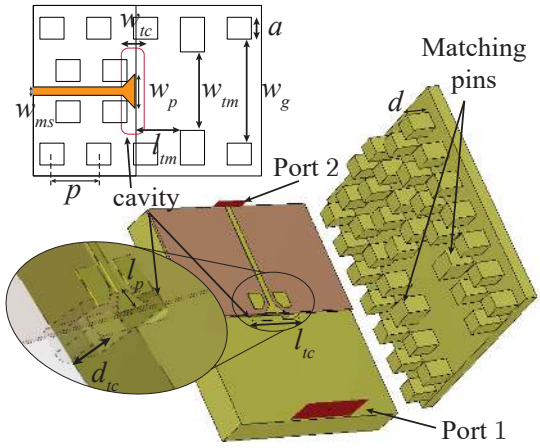

Fig. 21. Microstrip to groove gap waveguide transition geometry. (l_{tc} = 2.57 mm, w_{tc} = 0.62 mm, d_{tc} = 0.76 mm, w_g = 3.1 mm, w_{tm} = 2.34 mm, w_p = 1 mm, l_p = 0.33 mm, l_{tm} = 1.2 mm, a = 0.65 mm, d = 1 mm, and p = 1.26 mm)

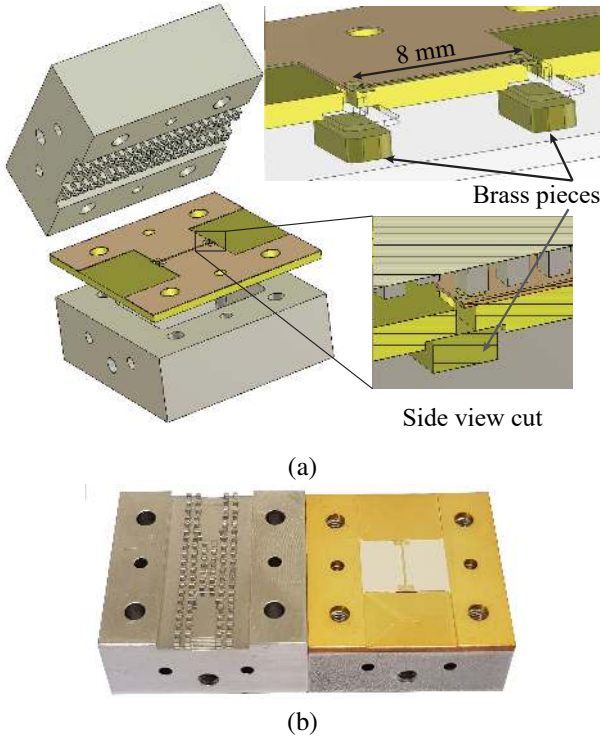

Fig. 22. (a) Configuration of back-to-back transition between microstrip line and GGW. (b) Fabricated back-to-back microstrip to GGW transition prototype.

tangent at millimeter wave frequency. The substrate consists of 50 μm Rogers Ultralam 3850HT and 50 μm Rogers Ultralam 3908 bonding film on a 1 mm copper plate. The PCB is gold plated afterwards to be able to apply wire-bonding. In [32], [33] the electrical properties of LCP substrate is measured and estimated, with a dielectric constant of 3.2 and a loss tangent of around 0.005 at 80 GHz. We have used these values in the modeling and all simulations.

The Tx and Rx MMICs have direct conversion architecture with differential IQ mixer based on GaAs technology. Differential IF (0-12 GHz) inputs/outputs and LO inputs (11.8-14.3 GHz) are provided with coaxial interfaces. The length of the microstrip lines that are connecting the IF coaxial connectors to the MMICs are equal to 90 mm and 42 mm for Tx and Rx, respectively. Furthermore, the LO path for the Tx and Rx MMICs are 35 mm and 47 mm long, respectively. The measured insertion loss of a 50 Ω microstrip line at 3 GHz and 15 GHz in [32] are estimated to be around 0.01 dB/mm and 0.04 dB/mm, respectively. Therefore, the maximum loss of 1.88 dB is expected for the Rx LO line (largest microstrip line at a higher frequency) at 15 GHz.

The LCP dielectric is removed around the footprint of the diplexer, which is on the next layer of the module as explained before. The carrier board also includes the two metal steps of the GGW to RW transitions (Fig. 12). The arrangement of the different parts of the designed carrier board is illustrated in Fig. 20. In this section, the detailed design of the main building blocks of the carrier board, such as a transition from the microstrip line to GGW and a compensation network for wire-bond interconnection, are presented. Moreover, the performance of the packaged Tx and Rx MMICs is also evaluated.

A. Microstrip to GGW transition design

Fig. 21 shows the designed transition between a microstrip line to the GGW. Similar transitions with different arrangement are presented in [34] and [35] at V- and W-band, respectively. The proposed transition is formed in two distinct parts, where the energy from the microstrip line couples to the GGW via a resonant cavity. The GGW line is created by a pin texture on the upper layer and a lid on the lower layer. The substrate is LCP (ϵ_r=3.2) with the thickness of 100 μm. An E-plane probe is extended into the cavity and the quasi-TEM mode of the microstrip is matched to TE_{10} mode of GGW by using the resonant characteristic of the cavity. The length of the cavity is around $\lambda_g/2$ at the lower operating frequency (70 GHz). The cavity has been made within the 1 mm thick copper plate. The copper plate acts as the ground plane of the microstrip line and the top lid of GGW. Two pins in the upper layer with a

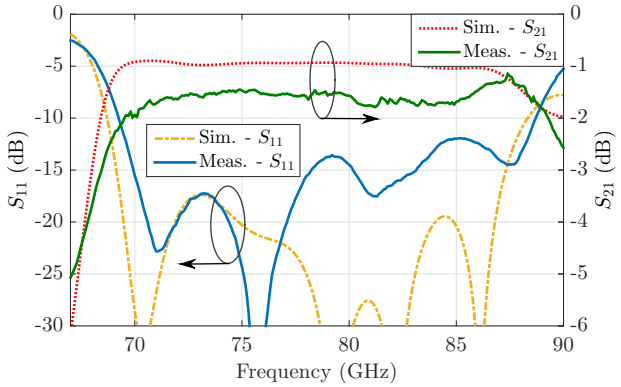

Fig. 23. Simulated and measured performance of back-to-back microstrip to GGW transition.

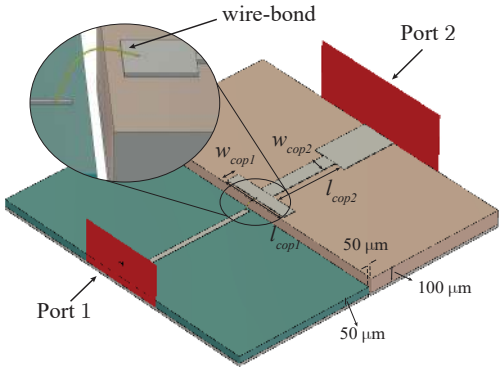

Fig. 24. Configuration of compensation matching network for wire-bond interconnection. ($l_{cop1} = 0.48$ mm, $w_{cop1} = 0.09$ mm, $l_{cop2} = 0.49$ mm, and $w_{cop2} = 0.1$ mm)

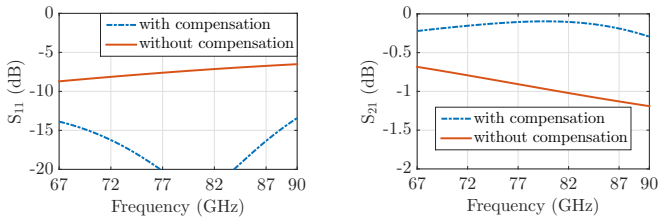

(a) (b)

Fig. 25. Simulated S-parameters of wire-bonded 50 μm microstrip lines in GaAs and LCP substrates with and without compensation. (a) Reflection coefficient. (b) Transmission coefficient.

distance of around $\lambda_g/4$ at the lower operating frequency from the E-plane probe are extended into the waveguide channel in order to add an extra reflection and improve the impedance matching of the transition. The dimensions of the cavity, the position of the E-plane probe, and the position and length of the matching pins are optimized to achieve a broadband impedance matching. The detailed geometry of the transition is illustrated in Fig. 21 with the optimized parameter values.

A back-to-back transition is fabricated in order to verify the performance of the designed transition. Fig. 22 shows the geometry of the back-to-back transition and the fabricated prototype. The pin texture in the upper layer, that forms the groove gap waveguide line, is fabricated in aluminum with CNC machining. An 8 mm long microstrip line is fabricated on 100 μm LCP substrate with 1mm thick copper base. To simplify the fabrication, the cavities are realized by first making through holes with the required dimensions in the 1 mm copper plate, and afterwards the holes are closed from the backside with small metal pieces. We have used brass pieces and conductive silver paste to enclose the holes and form the cavities, as shown in Fig. 22(a).

The simulated and measured performance of the fabricated back-to-back transition is shown in Fig. 23. The measured reflection coefficient is below -12 dB over the frequency band 69-87 GHz. The fabricated prototype shows higher insertion loss than the simulation. A measured average insertion loss of 1.5 dB (including the losses in the 8 mm microstrip line) has been achieved over the frequency band 71-86 GHz, where the simulated insertion loss is 1 dB over the same frequency band. The extra loss could be due to the enclosure of the cavities with conductive silver paste and extra substrate losses. The measured results in [32] shows that the insertion loss of a 50 Ω microstrip line on a 100 μm LCP substrate is around 0.11 dB/mm at 80 GHz. Therefore, by subtracting the loss of the 8 mm microstrip line of the fabricated back-to-back transition, the measured insertion loss of a single transition is estimated to be around 0.31 dB.

B. Wire-bond compensation network for TX/RX MMIC to board interconnection

Wire bonding is a conventional interconnection approach to electrically connect MMIC to microstrip or coplanar waveguide (CPW) transmission lines. However, using this approach becomes tricky by increasing the operating frequency. The wire-bond introduces an extra inductance that needs to be compensated in order to achieve a proper impedance matching, especially at high frequencies. Fig. 24 shows the matching section that we have used to compensate the wire-bond effect. A T-shape microstrip section with a capacitive impedance is used to compensate the inductance that is introduced by wire-bonding. We have assumed that a 50 Ω microstrip line on a 50 μm GaAs substrate (ε_r = 12.5) is connected to a microstrip line on a 100 μm substrate with a dielectric constant of 3.25 by a low profile wire-bond. The simulated S-parameters with and without compensation are presented in Fig. 25. The materials are considered loss-less, and the losses in Fig. 25 (b) are only due to mismatch and radiation losses. Fig. 25 (a) shows that the reflection coefficient improves from around -8 dB to below -15 dB over the frequency band 70-88 GHz by using the compensation matching network.

C. Tx and Rx modules performance

The performance of the Tx and Rx MMICs are measured to characterize and evaluate the packaging and assembly. The measurement setup is shown in Fig. 26. The IF and LO are provided by a Keysight N5241A PNA-X network analyzer and RF input/output is connected to a VDI WR-12 extender. The IF port from the network analyzer is connected to a 180° hybrid coupler which provides two out-of-phase outputs with equal amplitude. The outputs of the 180° hybrid are connected to two 90° hybrid couplers to provide differential

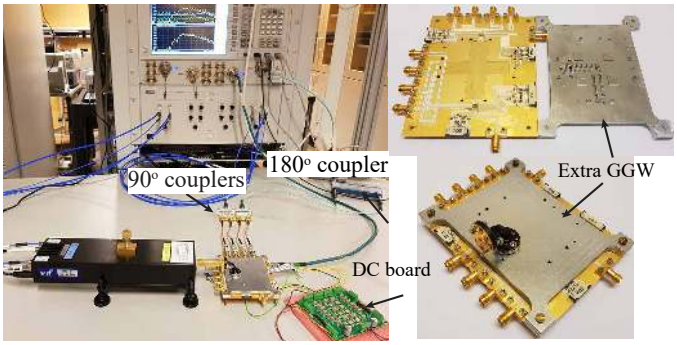

Fig. 26. Tx and Rx MMICs performance evaluation measurement setup.

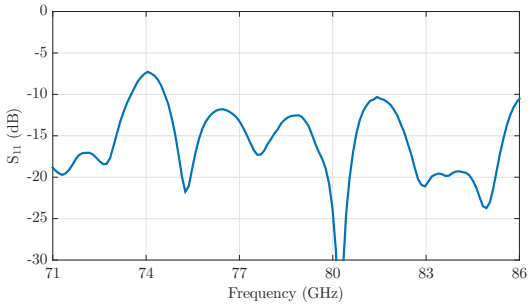

Fig. 27. Measured small signal reflection coefficient at output of Tx.

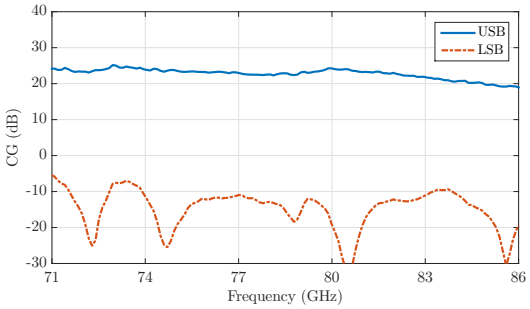

Fig. 28. Measured conversion gain of the signal (upper sideband) and the image (lower sideband) versus frequency of Tx for IF (3 GHz, -15 dBm) and LO (8 dBm).

IQ for input/output of Tx/Rx modules. An extra part with a GGW line is also fabricated for measurement purposes. The RF output/input of the Tx/Rx module is coupled to the GGW line via the microstrip to GGW transition, and afterwards to a WR-12 rectangular waveguide, as shown in Fig. 26. In the presented measurement results of this section, the losses due to the IF and LO microstrip lines on the PCB board, the microstrip to GGW transition, wire-bond, and the GGW to rectangular waveguide transition are included.

Fig. 27 shows small signal output matching of the Tx. The measured conversion gains of upper sideband (USB) and lower sideband (LSB) of the Tx are shown in Fig. 28. We have used a fixed IF of 3 GHz with an output power of −15 dBm and swept the LO frequency with LO output power of 8 dBm in these measurements. The measurement results show an average 23 dB conversion gain with good flatness and a measured image rejection of more than 30 dB over the

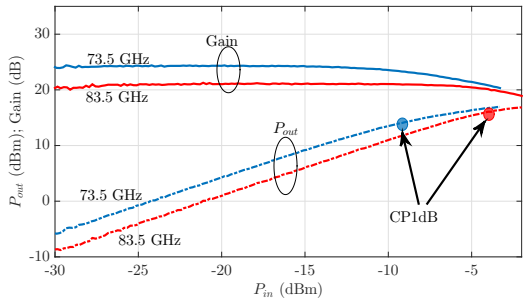

Fig. 29. Measured conversion gain and output power of Tx versus input power at 73.5 GHz and 83.5 GHz.

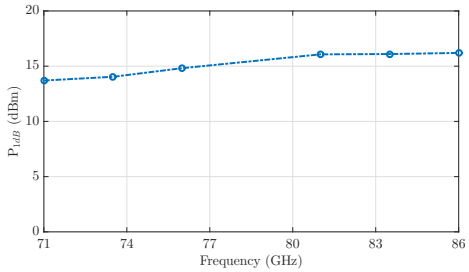

Fig. 30. Measured output power of Tx at 1-dB gain compression point versus frequency.

TABLE III
SUMMARY OF THE MEASURED PERFORMANCE OF THE INTEGRATED RADIO FRONT-END

Parameter	71-76 GHz	81-86 GHz
Diplexer insertion loss (dB)	0.5	0.5
Antennas+diplexer gain (dBi)	31	31.5
Microstrip to GGW transition loss (dB)	0.31	0.31
Transmitter gain (dB)	24	21
Transmitter P_{1dB} (dBm)	14	16
Receiver gain (dB)	20	24
Receiver noise figure (dB) *	5.5	5.5

* on-wafer measurements

frequency band of 71-86 GHz.

The measured output power and gain of the Tx module versus input power at 73.5 GHz and 83.5 GHz are presented in Fig. 29. The results show gains of 24 dB and 21 dB at 73.5 GHz and 83.5 GHz, respectively. The 1-dB gain compression points are also illustrated, with an input power at -9 dBm and -4 dBm at 73.5 GHz and 83.5 GHz respectively. The measured output power of the Tx at 1-dB gain compression versus frequency is presented in Fig. 30. The Tx module provides a high P_{1dB} output power around 14 dBm at 71-76 GHz, and 16 dBm at 81-86 GHz frequency bands.

The small signal RF input reflection coefficients of the two Rx MMICs on two carrier boards are shown in Fig. 31. The measured conversion gains of the Rx modules for IF frequency of 3 GHz and LO power of 8 dBm are shown in Fig. 32. Fig. 32(a) shows a measured conversion gain of 20 dB with an image rejection of more than 20 dB over the frequency band of 71-76 GHz. Similarly, the measured conversion gain of 24 dB and image rejection of 30 dB have been obtained for

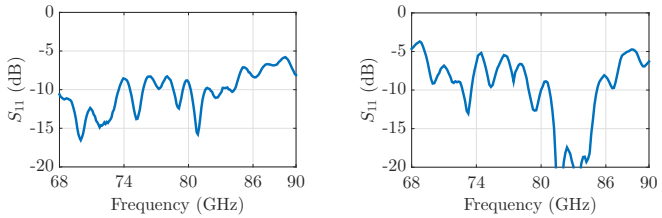

Fig. 31. Measured small signal reflection coefficient at the input of Rx. (a) Lower band (71-76 GHz) receiver. (b) Upper band (81-86 GHz) receiver.

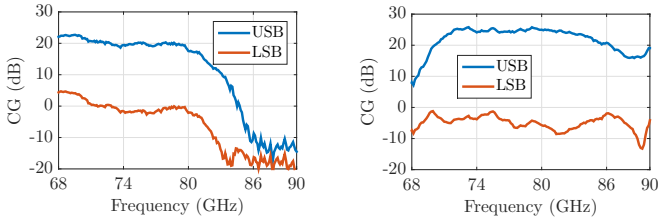

Fig. 32. Measured conversion gain of the signal (upper sideband) and the image (lower sideband) versus frequency of Rx for IF at 3 GHz, RF input power of -40 dBm, and LO power of 8 dBm. (a) Lower band (71-76 GHz) receiver. (b) Upper band (81-86 GHz) receiver.

the other Rx MMIC over the frequency band of 81-86 GHz.

VI. Wireless Link Demonstration

The designed module has the ability of full duplex wireless communication, i.e., to transmit in 71-76 GHz or 81-86 GHz bands, and receive in one of the lower or upper bands depending on which Rx MMIC is used in the carrier board. We have fabricated two integrated radio front-end modules, one with gRSC0012 MMIC to receive in the 71-76 GHz frequency band, and another one with gRSC0013 chipset to receive in the 81-86 GHz band. A summary of the measured performance of the fabricated prototypes is presented in Table III.

A. Link budget analysis

Based on the characterized performance in Table III, the link budget analysis can be done by calculating the received signal power given by (6) and the noise power given by (7) at the receiver input.

$$P_{sig} = P_{Tx} + 2 \times G_{Ant} - L_{FS} - L_{Rain} - L_{Atm} - L_M \quad (6)$$

$$P_{noise} = 10log_{10}(kTB) + NF_{Rx} \ (-75.9 \ @ \ B{=}1.8 \ GHz) \quad (7)$$

where P_{Tx} is the transmitter output power, G_{Ant} is the Tx and Rx antenna gain, L_{FS} is the free space path loss given by (8), L_{Rain} is the loss due to rain (16.4 dB for 40 mm/h), L_{Atm} is the atmospheric attenuation (0.4 dB/km), L_M is margin (4 dB as suggested in [36] for the 71-86 GHz band), k is the Boltzmann's constant ($1.38{\times}10^{-23}$ W/(K.Hz)), T is the background temperature (290 K), B is the transmitted signal bandwidth, and NF_{Rx} is the receiver's noise figure.

$$L_{FS} = 20log_{10}(d_{[km]}) + 20log_{10}(f_{[GHz]}) + 92.45 \quad (8)$$

For a transmitting signal with 1.8 GHz bandwidth, a maximum hop-length (d) of around 500 m is expected for 16-QAM modulation with theoretical Signal-to-Noise Ratio (SNR) of 20.5 dB at a bit error rate (BER) of 10^{-6} [36]. We have considered 4 dB coding gain [36] and 16.4 dB loss due to rain in this calculation. The spectral efficiency can be improved by using higher modulation schemes. However, the hop-length needs to be reduced in order to achieve the required higher SNR. For a 64-QAM modulation, to obtain a BER of 10^{-6} an SNR of 26.5 dB is required [36]. This decreases the expected hop-length to 200 m by considering 7 dB back-off in P_{1dB} output power of the Tx to have the required linearity.

TABLE IV
Summary of Over-The-Air Data Transmission Test.

Freq. (GHz)	Symb. rate (MBd/s)	Bandwidth (MHz)	Modulation	Data Rate (Gbit/s)	MSE* (dB)
73.5	666	750	64-QAM	3.99	-30.1
			128-QAM	4.66	-29.9
	888	1000	32-QAM	4.44	-25.9
			64-QAM	5.33	-25.7
	1599	1800	16-QAM	6.39	-22.7
			32-QAM	7.99	-22.5
83.5	666	750	64-QAM	3.99	-30
			128-QAM	4.66	-29.9
	888	1000	32-QAM	5.44	-25.9
			64-QAM	5.33	-25.8
	1599	1800	16-QAM	6.39	-22.6
			32-QAM	7.99	-22.4

* Mean Squared Error

B. Real-time multi-Gbit/s data transmission

A real-time wireless data transmission has been performed by sending single sideband (SSB) RF signal. The experimental setup is shown in Fig. 33. QAM modulated IQ signals at 3.5 GHz center IF frequency are produced by a modem. The Tx IF ports of the radio front-end module are first combined by 180° couplers to achieve single ended ports for the I and the Q channels. Then the I/Q channels are connected with a 90° coupler to separate upper/lower sidebands. The LO frequency is provided by an Agilent E8257D signal generator. The integrated radio front-end module up-converts and transmits the USB RF signals at center frequencies of 73.5 GHz and 83.5 GHz by LO at 11.67 GHz and 13.33 GHz, respectively. Another module receives and down-converts the signal to IF centered at 2 GHz. The Rx IF ports are combined with hybrid couplers and then connected to a similar modem. A separate signal generator is used for the RX module to provide LO at 11.92 GHz and 13.58 GHz for RF signals center frequencies of 73.5 GHz and 83.5 GHz, respectively. The two modules are separated by 25 m in indoor environment. Several modulation formats and symbol rates were tested at different frequencies.

A summarized measured link performance for different modulation schemes is presented in Table IV. A maximum

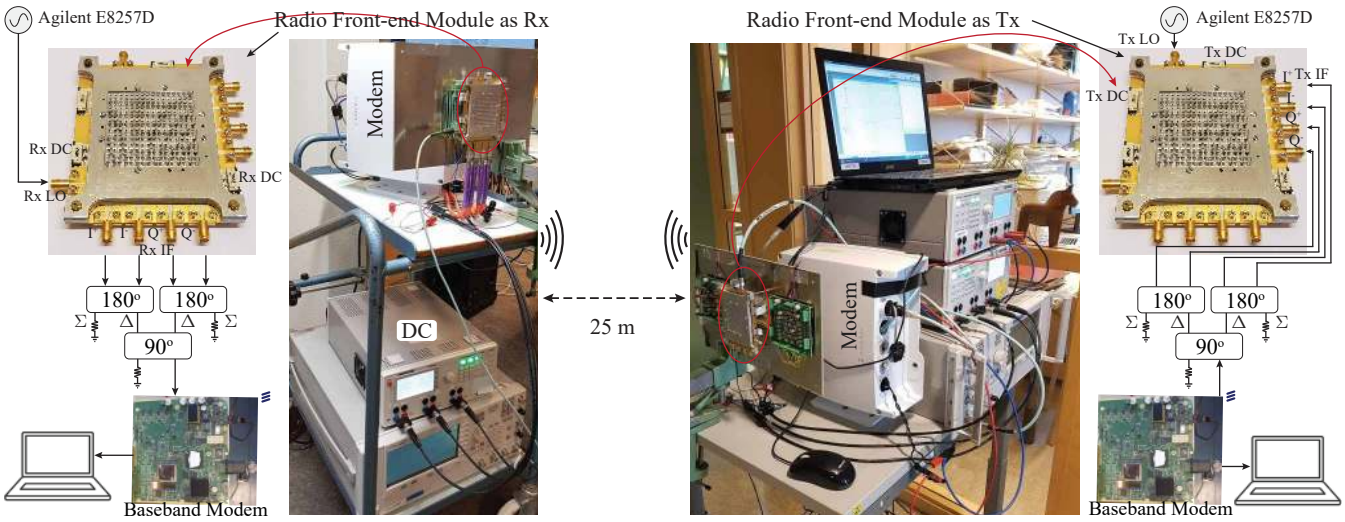

Fig. 33. Real-time data transmission test setup.

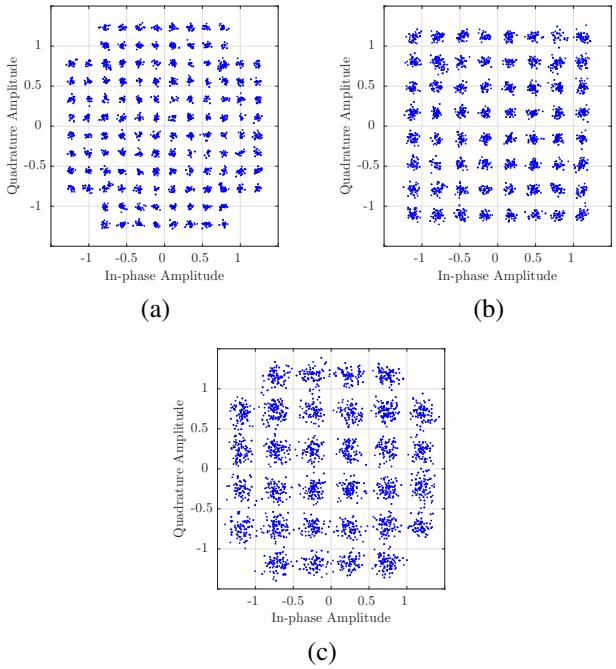

Fig. 34. Constellation diagrams of the received signal. (a) 128-QAM with 4.66 Gbit/s at 73.5 GHz, (b) 64-QAM with 5.33 Gbit/s at 83.5 GHz, and (c) 32-QAM with 8 Gbit/s at 83.5 GHz.

data rate of 8 Gbit/s is achieved by using 32-QAM modulation with spectral efficiency of 4.44 b/s/Hz. Fig. 34 also presents constellation diagrams for different modulations schemes. A comparison with some published articles has been presented in Table V. In all published works in Table V a wireless link and data transmission are demonstrated by either using bench-test measurement setup, or by designing the circuitry, packaging, diplexer, and antenna in separate modules, which increase the cost and size of the system.

TABLE V
COMPARISON BETWEEN STATE-OF-THE-ART E-BAND MULTI-GBIT/S DATA TRANSMISSION.

Ref	Test setup	Data rate-Modulation	Spectral eff. (bit/s/Hz
[4] (SiGe)	bench test	10.12 (Gbit/s) 64-QAM	5.06
[5] (GaAs)	bench test	6 (Gbit/s) 8PSK	2.4
[6] (n. a.)	bench test	10 (Gbit/s) 16-QAM	2
[7] (SiGe)	bench test	20 (Gbit/s) 32-QAM	<5
[37] (GaAs)	link	10 (Gbit/s) 16-QAM	3.2
This work (GaAs)	real-time link	8 (Gbit/s) 32-QAM	4.44

VII. CONCLUSION

A compact integrated solution for multi-Gbit/s data transmission for point-to-point wireless link applications at E-band has been presented. A full-duplex FDD radio front-end module has been designed by integrating a high gain array antenna, a diplexer, and RF circuitry consisting of Tx/Rx MMICs in one package. The proposed solution has a novel architecture, consisting of four vertically stacked layers with a simple mechanical assembly. This is due to the use of gap waveguide technology, which eliminates electrical and galvanic contact requirement in waveguide structures and provides an effective system packaging solution.

The performance of each building block of the designed module has initially been evaluated separately, and then two integrated modules have been used to demonstrate a multi-gigabit data transmission. The measurement results show that the integrated antenna-diplexer prototype has a gain of more than 31 dBi with an antenna efficiency better than 65%, where 0.5 dB loss is due to the diplexer. A maximum data rate of 8 Gbit/s was achieved by sending a 32-QAM modulated signal over a distance of 25 m, with spectral

efficiency of 4.44 bit/s/Hz. Based on the summarized measured performance of the fabricated modules given in Table III, for different modulations of 16-QAM and 64-QAM the hop-length of around 500 m and 200 m is expected with 1.8 GHz channel bandwidth. The proposed integrated module has the ability to send and receive data simultaneously by using an FDD transmission scheme. A maximum data rate of 16 Gbit/s can be achieved by using the full potential of the designed module.

The proposed integrated radio front-end module shows the mechanical flexibility and great potential of the gap waveguide technology in system integration and packaging with high complexity.

ACKNOWLEDGMENT

The authors would like to thank Gapwaves AB for producing the metal waveguide structures, Gotmic AB for providing the Tx/Rx MMICs, and Ericsson Research (Göteborg) for modems used within this work.

REFERENCES

[1] D. Lockie and D. Peck, "High-data-rate millimeter-wave radios," *IEEE Microw. Mag.*, vol. 10, no. 5, 2009.

[2] J. Hansryd, Y. Li, J. Chen, and P. Ligander, "Long term path attenuation measurement of the 71–76 GHz band in a 70/80 GHz microwave link," in *Proc. of the 4th European Conf. on Antennas and Propag. (EuCAP)*. Barcelona, 2010.

[3] "Specific attenuation model for rain for use in prediction methods," ITU-R Recommendations, ITU-R P.8383-3, Geneva, Switzerland, 2005.

[4] del Rio *et al.*, "A wideband and high-linearity E-band transmitter integrated in a 55-nm SiGe technology for backhaul point-to-point 10-Gb/s links," *IEEE Trans. Microw. Theory Techn.*, vol. 65, no. 8, pp. 2990–3001, 2017.

[5] V. Dyadyuk *et al.*, "A multigigabit millimeter-wave communication system with improved spectral efficiency," *IEEE Trans. Microw. Theory Techn.*, vol. 55, no. 12, pp. 2813–2821, 2007.

[6] J. Chen *et al.*, "10 Gbps 16QAM transmission over a 70/80 GHz (E-band) radio test-bed," in *Proc. of the 7th European Microw. Integr. Circuits Conf. (EuMIC)*, 2012, pp. 556–559.

[7] S. Trotta *et al.*, "A V and E-band packaged direct-conversion transceiver chipset for mobile backhaul application in SiGe technology," in *Proc. of the 11th European Radar Conf. (EuRAD)*, 2014, pp. 352–355.

[8] P.-S. Kildal, "Artificially soft and hard surfaces in electromagnetics," *IEEE Trans. Antennas Propag.*, vol. 38, no. 10, pp. 1537–1544, 1990.

[9] P.-S. Kildal, A. U. Zaman, E. Rajo-Iglesias, E. Alfonso, and A. Valero-Nogueira, "Design and experimental verification of ridge gap waveguide in bed of nails for parallel-plate mode suppression," *IEEE Microw. Antennas Propag. Lett.*, vol. 5, no. 3, pp. 262–270, Feb. 2011.

[10] E. Rajo-Iglesias and P.-S. Kildal, "Groove gap waveguide: A rectangular waveguide between contactless metal plates enabled by parallel-plate cut-off," in *Proc. of the 4th European Conf. on Antennas and Propag. (EuCAP)*. Barcelona, 2010, pp. 1–4.

[11] A. A. Brazález, E. Rajo-Iglesias, J. L. Vazquez-Roy, A. Vosoogh, and P.-S. Kildal, "Design and validation of microstrip gap waveguides and their transitions to rectangular waveguide, for millimeter-wave applications," *IEEE Trans. Microw. Theory Techn.*, vol. 63, no. 12, pp. 4035–4050, 2015.

[12] A. Vosoogh, P.-S. Kildal, and V. Vassilev, "Wideband and high-gain corporate-fed gap waveguide slot array antenna with ETSI class II radiation pattern in V-band," *IEEE Trans. Antennas Propag.*, 2016.

[13] A. Vosoogh, P.-S. Kildal, V. Vassilev, A. U. Zaman, and S. Carlsson, "E-band 3-D metal printed wideband planar horn array antenna," in *Proc. of the 2016 Int. Symp. on Antennas and Propag. (ISAP)*. Okinawa, Jpn., 2016.

[14] A. Vosoogh and P.-S. Kildal, "Corporate-fed planar 60 GHz slot array made of three unconnected metal layers using AMC pin surface for the gap waveguide," *IEEE Antennas Wireless Propag. Lett.*, vol. 15, pp. 1935–1938, Dec. 2015.

[15] H. Attia, M. S. Sorkherizi, and A. A. Kishk, "60 GHz slot antenna array based on ridge gap waveguide technology enhanced with dielectric superstrate," in *Proc. of the 9th European Conf. on Antennas and Propag. (EuCAP)*. Lisbon, 2015, pp. 1–4.

[16] A. Vosoogh, P.-S. Kildal, and V. Vassilev, "A multi-layer gap waveguide array antenna suitable for manufactured by die-sink EDM," in *Proc. of the 10th European Conf. on Antennas and Propag. (EuCAP)*. Davos, 2016, pp. 1–4.

[17] A. Vosoogh, A. A. Brazález, and P.-S. Kildal, "A V-band inverted microstrip gap waveguide end-coupled bandpass filter," *IEEE Microw. Wireless Compon. Lett.*, vol. 26, no. 4, pp. 261–263, Apr. 2016.

[18] M. S. Sorkherizi, A. Khaleghi, and P.-S. Kildal, "Direct-coupled cavity filter in ridge gap waveguide," *IEEE Trans. Compon., Packag., Manuf. Technol.*, vol. 4, no. 3, pp. 490–495, Mar. 2014.

[19] A. Berenguer, M. Baquero-Escudero, D. Sanchez-Escuderos, B. Bernardo-Clemente, and V. E. Boria-Esbert, "Low insertion loss 61 GHz narrow-band filter implemented with groove gap waveguides," in *Proc. of the 44th European Microw. Conf. (EuMC)*, 2014, pp. 191–194.

[20] E. A. Alós, A. U. Zaman, and P.-S. Kildal, "Ka-band gap waveguide coupled-resonator filter for radio link diplexer application," *IEEE Trans. Compon., Packag., Manuf. Technol.*, vol. 3, no. 5, pp. 870–879, 2013.

[21] M. Rezaee, A. U. Zaman, and P.-S. Kildal, "V-band groove gap waveguide diplexer," in *Proc. of the 9th European Conf. on Antennas and Propag. (EuCAP)*. Lisbon, 2015, pp. 1–4.

[22] M. S. Sorkherizi and A. A. Kishk, "Fully printed gap waveguide with facilitated design properties," *IEEE Microw. Wireless Compon. Lett.*, vol. 26, no. 9, pp. 657–659, 2016.

[23] M. Rezaee, A. U. Zaman, and P.-S. Kildal, "A groove gap waveguide iris filter for V-band application," in *Proc. of the 23rd Iranian Conf. on Elect. Eng. (ICEE)*, 2015, pp. 462–465.

[24] M. S. Sorkherizi and A. A. Kishk, "Completely tuned coupled cavity filters in defected bed of nails cavity," *IEEE Trans. Compon., Packag., Manuf. Technol.*, 2016.

[25] A. Vosoogh, M. S. Sorkherizi, A. U. Zaman, J. Yang, and A. A. Kishk, "An integrated Ka-band diplexer-antenna array module based on gap waveguide technology with simple mechanical assembly and no electrical contact requirements," *IEEE Trans. Microw. Theory Techn.*, vol. 66, no. 2, pp. 962–972, 2018.

[26] ——, "An E-band antenna-diplexer compact integrated solution based on gap waveguide technology," in *Proc. of the 2017 Int. Symp. on Antennas and Propag. (ISAP)*. Phuket, 2017, pp. 1–2.

[27] ——, "Diplexer integration into a Ka-band high-gain gap waveguide corporate-fed slot array antenna," in *Proc. of the 2017 IEEE Int. Symp. on Antennas and Propag. (APSURSI)*, 2017, pp. 2667–2668.

[28] M. S. Sorkherizi, A. Vosoogh, A. A. Kishk, and P.-S. Kildal, "Design of integrated diplexer-power divider," in *Proc. of the 2016 IEEE MTT-S Int. Microw. Symp.* San Francisco, CA, USA, 2016, pp. 1–3.

[29] R. J. Cameron, C. M. Kudsia, and R. Mansour, *Microwave filters for communication systems*. John Wiley & Sons, 2015.

[30] M. S. Sorkherizi and A. A. Kishk, "Use of Group Delay of Sub-Circuits in Optimization of Wideband Large-Scale Bandpass Filters and Diplexers," *IEEE Trans. Microw. Theory Techn.*, 2017.

[31] J. W. Bandler, R. M. Biernacki, S. H. Chen, P. A. Grobelny, and R. H. Hemmers, "Space mapping technique for electromagnetic optimization," *IEEE Trans. Microw. Theory Techn.*, vol. 42, no. 12, pp. 2536–2544, 1994.

[32] D. C. Thompson, O. Tantot, H. Jallageas, G. E. Ponchak, M. M. Tentzeris, and J. Papapolymerou, "Characterization of liquid crystal polymer (LCP) material and transmission lines on LCP substrates from 30 to 110 GHz," *IEEE Trans. Microw. Theory Techn.*, vol. 52, no. 4, pp. 1343–1352, 2004.

[33] S. L. Smith and V. Dyadyuk, "Measurement of the dielectric properties of Rogers R/flex 3850 liquid crystalline polymer substrate in V and W band," in *Proc. of the 2005 IEEE Antennas and Propag. Soc. Int. Symp.*, vol. 4, 2005, pp. 435–438.

[34] U. Nandi, A. U. Zaman, A. Vosoogh, and J. Yang, "Novel millimeter wave transition from microstrip line to groove gap waveguide for MMIC packaging and antenna integration," *IEEE Microw. Wireless Compon. Lett.*, vol. 27, no. 8, pp. 691–693, 2017.

[35] A. U. Zaman, V. Vassilev, H. Zirath, and N. Rorsman, "Novel low-loss millimeter-wave transition from waveguide-to-microstrip line suitable for MMIC integration and packaging," *IEEE Microw. Wireless Compon. Lett.*, vol. 27, no. 12, pp. 1098–1100, 2017.

[36] *Fixed Radio Systems; Parameters affecting the Signal-to-Noise Ratio (SNR) and the Receiver Signal Level (RSL) threshold in point-to-point receivers; Theory and practice*, document ETSI TR 103 053 V1.1.1, 2014.

[37] M.-S. Kang, B.-S. Kim, K. S. Kim, W.-J. Byun, and H. C. Park, "16-QAM-based highly spectral-efficient E-band communication system with bit rate up to 10 Gbps," *ETRI journal*, vol. 34, no. 5, pp. 649–654, 2012.